optica

Diamond optomechanical crystals

Michael J. Burek,[1] Justin D. Cohen,[2] Seán M. Meenehan,[2] Nayera El-Sawah,[1,3] Cleaven Chia,[1] Thibaud Ruelle,[1,4] Srujan Meesala,[1] Jake Rochman,[1,3] Haig A. Atikian,[1] Matthew Markham,[5] Daniel J. Twitchen,[5] Mikhail D. Lukin,[6] Oskar Painter,[2] and Marko Lončar[1,*]

[1]John A. Paulson School of Engineering and Applied Sciences, Harvard University, 29 Oxford Street, Cambridge, Massachusetts 02138, USA
[2]Kavli Nanoscience Institute, Institute for Quantum Information and Matter and Thomas J. Watson, Sr., Laboratory of Applied Physics, California Institute of Technology, Pasadena, California 91125, USA
[3]University of Waterloo, 200 University Avenue West, Waterloo, Ontario N2L 3G1, Canada
[4]École Polytechnique Fédérale de Lausanne (EPFL), CH-1015 Lausanne, Switzerland
[5]Element Six Innovation, Fermi Avenue, Harwell Oxford, Didcot, Oxfordshire OX110QR, UK
[6]Department of Physics, Harvard University, 17 Oxford Street, Cambridge, Massachusetts 02138, USA
*Corresponding author: loncar@seas.harvard.edu

Received 2 September 2016; revised 23 October 2016; accepted 24 October 2016 (Doc. ID 275148); published 18 November 2016

Cavity-optomechanical systems realized in single-crystal diamond are poised to benefit from its extraordinary material properties, including low mechanical dissipation and a wide optical transparency window. Diamond is also rich in optically active defects, such as the nitrogen-vacancy (NV) and silicon-vacancy (SiV) centers, which behave as atom-like systems in the solid state. Predictions and observations of coherent coupling of the NV electronic spin to phonons via lattice strain have motivated the development of diamond nanomechanical devices aimed at the realization of hybrid quantum systems in which phonons provide an interface with diamond spins. In this work, we demonstrate diamond optomechanical crystals (OMCs), a device platform to enable such applications, wherein the co-localization of ∼200 THz photons and few to 10 GHz phonons in a quasi-periodic diamond nanostructure leads to coupling of an optical cavity field to a mechanical mode via radiation pressure. In contrast to other material systems, diamond OMCs operating in the resolved-sideband regime possess large intracavity photon capacities ($>10^5$) and sufficient optomechanical coupling rates to reach a cooperativity of ∼20 at room temperature, allowing for the observation of optomechanically induced transparency and the realization of large-amplitude optomechanical self-oscillations.

OCIS codes: (120.4880) Optomechanics; (140.4780) Optical resonators; (220.1920) Diamond machining; (230.0230) Optical devices.

http://dx.doi.org/10.1364/OPTICA.3.001404

1. INTRODUCTION

Optomechanical crystals (OMCs), first demonstrated in silicon [1] and later in other materials such as silicon nitride [2,3], aluminum nitride [4,5], and gallium arsenide [6,7], have emerged as a fruitful optomechanics platform, wherein radiation pressure effects provide exquisitely sensitive optical control of mechanical vibrations. Such systems have enabled demonstrations of quantum ground-state cooling [8], optomechanically induced transparency (OMIT) [9], squeezed light [10], and wavelength conversion [11]. Highly coherent photon–phonon interactions in OMCs are a direct result of the ability to engineer a large single-photon optomechanical coupling rate (g_o) while retaining sufficiently small optical (κ) and intrinsic mechanical (γ_i) dissipation rates. Similar structures realized in single-crystal diamond, which features a unique combination of superior mechanical, thermal, and optical properties [12], are expected to exhibit pronounced optomechanical interactions, quantified by the cooperativity parameter $C = 4n_c g_o^2/\kappa\gamma_i$ (where n_c is the intracavity photon number). Specifically, the wide bandgap of diamond (∼5.5 eV) precludes multi-photon absorption over a wide wavelength range (from visible to infrared). This, combined with their high thermal conductivity and small thermal expansion, enables monolithic diamond optical cavities that can withstand significant optical power densities, while avoiding degradation in optical linewidth or drifts in resonance wavelength due to thermal lensing. The large intracavity photon capacity of diamond can thus result in the high cooperativities necessary for either strong mechanical driving or effective laser cooling [8]. Moreover, diamond is among the stiffest materials known and possesses extremely low thermoelastic mechanical damping, with recently demonstrated monolithic diamond cantilevers exhibiting mechanical Q-factors in excess of 10^6 at room temperature [13]. In what follows, we make use of these features to demonstrate OMCs in single-crystal diamond with unique performance. Our diamond OMCs support an optical mode at $\omega_o/2\pi \sim 200$ THz, co-resonant with two localized acoustic phonon modes at $\omega_m/2\pi \sim 5.5$ and ∼9.5 GHz. Both mechanical resonances are well coupled to the optical cavity, with vacuum optomechanical coupling rates of

$g_o/2\pi \sim 120$ and ~220 kHz, respectively. With a measured optical linewidth of $\kappa/2\pi \sim 1.1$ GHz, our diamond OMC system operates in the so-called resolved sideband regime ($\omega_m/\kappa \gg 1$), necessary for efficient radiation-pressure-driven dynamic backaction. This enables our diamond OMCs to be optically driven to $C \gg 1$ at room temperature, highlighted by the observations of "phonon lasing" [14] and OMIT [9] in our structures.

2. DIAMOND OPTOMECHANICAL CRYSTAL DESIGN AND FABRICATION

The OMCs of this work consist of a one-dimensional nanobeam photonic crystal cavity fabricated in synthetic single-crystal diamond [15] using previously developed "angled-etching" techniques [16,17]. The nanobeam cavity is based on a diamond waveguide with a triangular cross-section that is perforated with a periodic lattice of elliptically shaped air holes. One unit cell of the waveguide and corresponding photonic band structure are shown in Figs. 1(a) and 1(b), respectively. The latter includes both transverse electric (TE-like, solid black lines) and transverse magnetic (TM-like, dashed blue lines) guided modes, while the gray shaded region indicates the continuum of radiation and leaky modes that exist above the light line for the structure. In this work, we focus on TE-like modes [see Fig. 1(b) inset] near the X-point frequency of $\omega_o/2\pi \sim 200$ THz ($\lambda \sim 1550$ nm), since they can lead to the realization of very high Q-factor optical cavities [15]. Importantly, our photonic crystal waveguide also supports acoustic guided modes that spatially overlap with optical modes and can couple to them via radiation pressure. The corresponding mechanical band structure [Fig. 1(c)] reveals a rich library of guided acoustic modes in the few to ~12 GHz frequency range (see Supplement 1 for extended discussions [18]). The guided modes, categorized by even (solid black lines) and odd (dashed blue lines) vector symmetries about the xz-plane, yield symmetry-based quasi-bandgaps. Following OMC design rules [19,20], we identified the guided modes derived from the Γ-point of the fourth and seventh y-symmetric bands (frequencies of $\omega_m/2\pi \sim 6.9$ and ~11.5 GHz), referred to hereafter as the "flapping" and "swelling" acoustic guided modes [Figs. 1(d) and 1(e)], respectively, as the mechanical modes of interest for large optomechanical coupling. To produce an optimized diamond OMC design, we focus on the acoustic flapping mode due to the large quasi-bandgap below its native band, which is indicated by the shaded pink region in Fig. 1(c).

To realize a diamond OMC cavity from the aforementioned OMC waveguide, the lattice of air holes is chirped [19] so as to transition from a "mirror" region formed by the base unit cell in Fig. 1(a) to a "defect" cell. The selected defect cell dimensions simultaneously raise and lower the frequencies of the target optical and mechanical modes, respectively, into their corresponding quasi-bandgaps. Gradually reducing the unit cell lattice constant while also decreasing the air hole aspect ratio (h_y/h_x) achieves the necessary band-edge tuning [see the right and left panels of Figs. 1(b) and 1(c), respectively]. An optimized design [18] was determined via numerical optimization methods based on FEM simulations (COMSOL) to calculate the optical (ω_o) and mechanical (ω_m) cavity resonance frequencies, the optical Q-factor (Q_o), and g_o. Both the moving boundary ($g_{o,\mathrm{MB}}$) and photoelastic ($g_{o,\mathrm{PE}}$) contributions to the single-photon optomechanical coupling rate were considered [18], with the calculation of $g_{o,\mathrm{PE}}$ performed using the following photoelastic coefficients of diamond [21]: $(p_{11}, p_{12}, p_{44}) = (-0.25, 0.043, -0.172)$. The normalized electric field (E_y) and mechanical displacement profiles (xy plane) of the final optimized diamond OMC design are shown in Figs. 1(f) and 1(g), respectively. The optimized design,

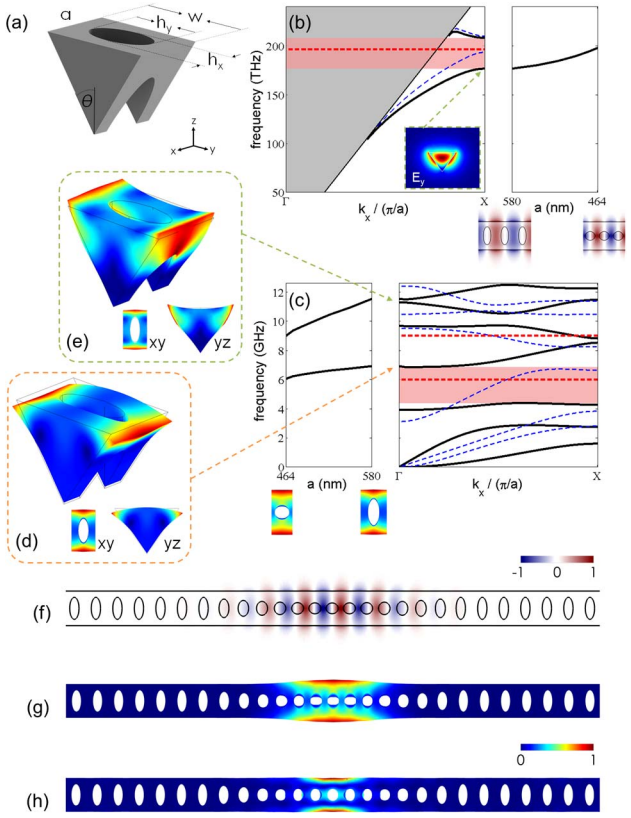

Fig. 1. Diamond optomechanical crystal optimized design. (a) Solid model representation of the triangular cross-section unit cell, which is parameterized by the etch angle (θ), width (w), lattice constant (a), and elliptical air hole diameters (h_x, h_y). Corresponding (b) optical and (c) mechanical band structures of a nominal diamond unit cell with $\theta = 35°$ and $(a, w, h_x, h_y) = (580, 929, 250, 590)$ nm. Below the light line in (b), supported transverse electric (TE-like) and transverse magnetic (TM-like) guided modes are indicated by solid black and dashed blue lines, respectively. The left panel inset of (b) displays the cross-sectional optical E_y-field profile of the first (dielectric) TE-like guided optical mode at the X-point. In (c), mechanical guided modes shown are for propagation along the x-axis, with y-symmetric and y-antisymmetric vector symmetries again indicated by solid black and dashed blue lines, respectively. Mechanical simulations assume guided mode propagation is oriented with the in-plane [110] crystallographic direction, with the z-axis oriented along [001]. The pink shaded regions in (b) and (c) highlight the optical and mechanical symmetry bandgaps of interest, respectively. Three-dimensional mechanical displacement profiles of the acoustic (d) "flapping" and (e) "swelling" guided modes originating from the Γ-point of the fourth and seventh y-symmetric bands, respectively. The right and left panels in (b) and (c), respectively, show the tuning of the X-point optical and Γ-point mechanical modes of interest as the unit cell is transitioned smoothly from the nominal unit cell to a defect cell with a reduced lattice constant and decreased air hole eccentricity, specifically, $(a_{\mathrm{defect}}, h_{x,\mathrm{defect}}, h_{y,\mathrm{defect}}) = (464, 327, 289)$ nm. Normalized (e) optical E_y-field of the localized optical cavity mode and mechanical displacement profiles of the (f) flapping and (g) swelling mechanical cavity modes for the optimized diamond OMC design. Eigenfrequencies of these localized optical and mechanical modes are indicated on the respective band structures in (b) and (c) by dashed red lines.

which assumes the x-axis orientation is aligned with the in-plane diamond [110] crystallographic direction, has an optical resonance at $\omega_o/2\pi = 196$ THz ($\lambda_o = 1529$ nm), a radiation-limited optical Q-factor of 7.4×10^5, a mode volume of $0.57(\lambda/n)^3$, an acoustic flapping mode mechanical resonance at $\omega_m/2\pi = 6.18$ GHz, and zero-point motion of $x_{zpf} = 3.1$ fm. The final coupling rate for this design was $g_o/2\pi = 136$ kHz and included a moving boundary and photoelastic contribution of $g_{o,MB}/2\pi = 62$ kHz and $g_{o,PE}/2\pi = 74$ kHz, respectively.

With our final diamond OMC design optimized for the acoustic flapping mode, we also observe a localization of the previously mentioned acoustic swelling mode [displacement profile shown in Fig. 1(h)] at a mechanical frequency of $\omega_m/2\pi = 9.01$ GHz, with a zero-point motion of $x_{zpf} = 2.2$ fm. The simulated optomechanical coupling rate for this design was $g_o/2\pi = 234$ kHz, which includes a moving boundary and photoelastic contribution of $g_{o,MB}/2\pi = 50$ kHz and $g_{o,PE}/2\pi = 184$ kHz, respectively. We attribute the overall greater optomechanical coupling rate of the acoustic swelling mode to its cross-sectional strain profile, which more favorably overlaps with the TE-like optical mode. While this mode is better coupled to the localized optical cavity, its predicted mechanical resonance frequency is not fully isolated within a symmetry-based quasi-bandgap [see Fig. 1(c)], which may ultimately limit its mechanical Q-factor in fabricated structures [1,20].

As previously mentioned, the fabrication of the diamond OMCs utilized angled-etching techniques [15–18] [as illustrated in Fig. 2(a)], which employ anisotropic oxygen-based plasma etching at an oblique angle to the substrate surface, resulting in suspended structures with a triangular cross-section. The final fabricated structures, displayed in Figs. 2(b)–2(d), reveal excellent reproductions of the intended design. A unique feature of angled-etched structures is their triangular cross-sectional symmetry [18]. The high-resolution SEM image shown in Fig. 2(e) reveals a fabricated diamond OMC (oriented upside down), with the insets displaying a tilted cross-sectional view.

3. OPTICAL AND MECHANICAL SPECTROSCOPY

The fiber-optical characterization setup [18] used to perform both optical and mechanical spectroscopy of diamond OMCs is schematically displayed in Fig. 3(a). Briefly, light from a tunable laser source (TLS) was evanescently coupled to the device under test via a dimpled fiber taper. A small portion of laser signal fed to a wavemeter enabled continuous monitoring of the laser frequency. An erbium-doped fiber amplifier (EDFA) was used in certain experiments to increase the maximum input laser power, and a variable optical attenuator (VOA) was used to set the final laser power delivered to the device. The optical cavity transmission spectrum was collected by a low-speed (125 MHz) photodetector, while a high-speed (12 GHz) photoreceiver monitored the radio frequency (RF) response of the mechanical cavity via a real-time spectrum analyzer (RSA). For the OMIT measurements discussed later in this work, an electro-optic phase modulator (EOPM), placed in the input fiber path, was used to create a weak tunable probe signal on the pump-laser control field. Port 1 of a high-frequency vector network analyzer (VNA) supplied the RF input to the EOPM, while port 2 of the VNA collected the RF output of the high-speed photoreceiver. All measurements were performed at room temperature and under ambient pressure.

A transmission spectrum of a representative diamond OMC, displayed in Fig. 3(b), reveals the optical cavity resonance centered at $\lambda_o = 1529.2$ nm, with a measured total and intrinsic optical Q-factor of $Q_t \sim 1.76 \times 10^5$ and $Q_i \sim 2.70 \times 10^5$, respectively. The corresponding total cavity decay rate, fiber taper coupling rate, and intrinsic optical decay rate are $\kappa/2\pi = 1.114$ GHz, $\kappa_e/2\pi = 399$ MHz, and $\kappa_i/2\pi = 715$ MHz, respectively. With the input laser slightly detuned from the optical cavity, the broadband RF spectrum of thermally excited motion at room temperature (i.e., thermal Brownian motion) reveals a series of mechanical resonances [18], as shown in the normalized power spectral density (NPSD) in Fig. 3(c). Specifically, we attribute the sharp resonance observed at ~5.5 GHz to the diamond OMC acoustic flapping mode. A high-resolution RF spectrum [shown

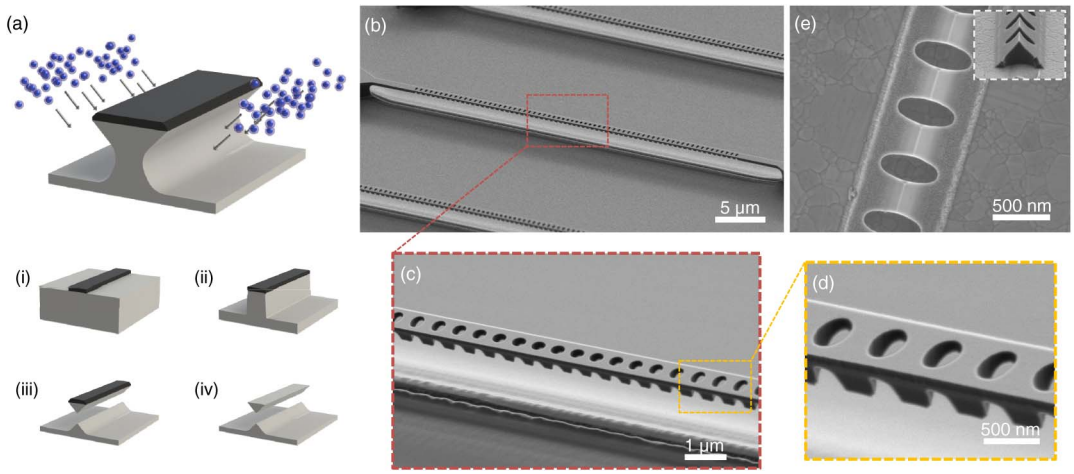

Fig. 2. Fabricated diamond optomechanical crystals. (a) Illustration of angled etching used to realize diamond OMCs. Angled-etching nanofabrication steps: (i) define an etch mask on a substrate via standard fabrication techniques, (ii) transfer etch mask pattern onto the substrate by conventional top-down plasma etching, (iii) employ angled etching to realize suspended nanobeam structures (see illustration), and (iv) remove residual etch mask. SEM images of (b) a fabricated diamond OMC, (c) zoomed-in view of the defect region, and (d) high-resolution image of fabricated air holes comprising the Bragg mirror region. (e) SEM image of an (inverted) diamond OMC liberated from the diamond substrate via stamping on a silver-coated silicon wafer. Inset shows a tilted (60°) SEM image of a broken diamond OMC, revealing the triangular cross-section.

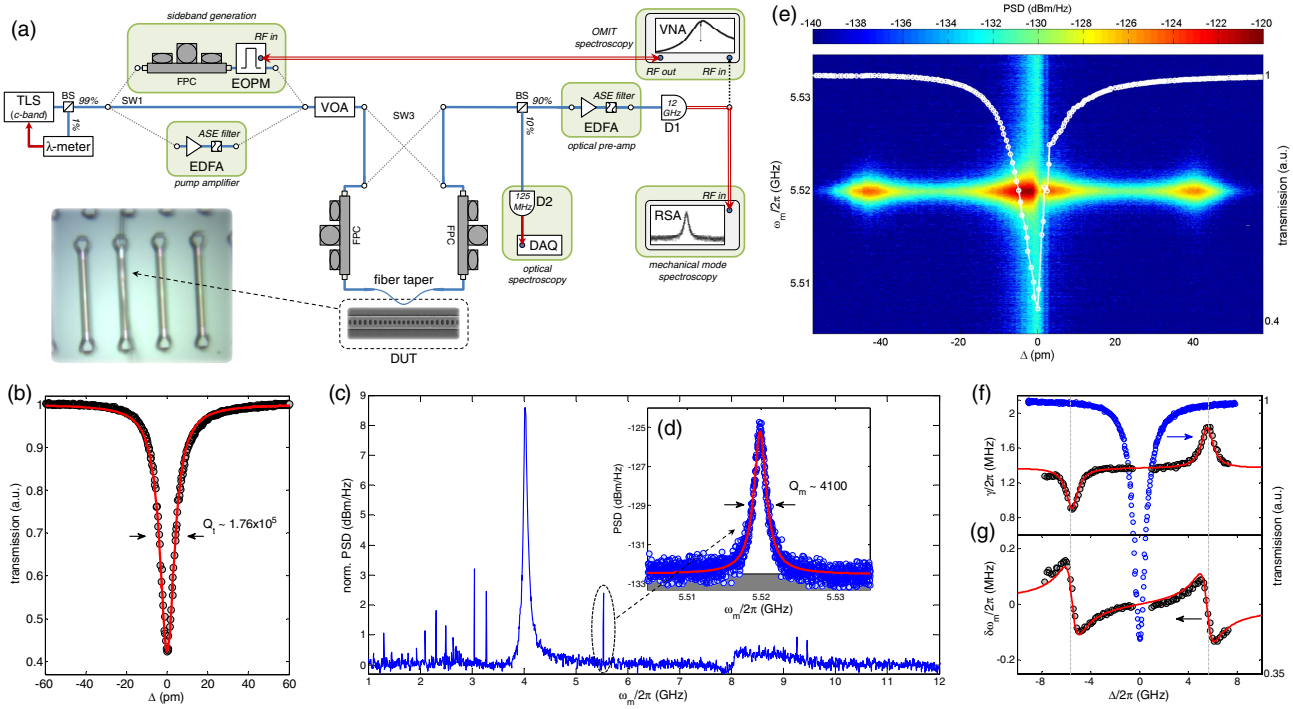

Fig. 3. Diamond optomechanical crystal optical and mechanical mode spectroscopy. (a) Schematic of the fiber-optical characterization setup (see Supplement 1 for description of symbols). The inset is an optical micrograph of the dimpled fiber taper in contact with the diamond OMC under test. (b) Normalized optical transmission spectrum, centered at $\lambda_o = 1529.2$ nm ($\omega_o/2\pi = 196$ THz), of a representative diamond OMC. A Lorentzian fit (solid red curve) yields a measured optical Q-factor of 1.76×10^5, corresponding to an optical linewidth of $\kappa \sim 1.11$ GHz. (c) Normalized power spectral density (PSD) revealing the broadband radio frequency spectrum of optically transduced diamond OMC thermal Brownian motion (at room temperature). Sharp resonances are attributed to various localized and extended acoustic phonon modes of the diamond OMC [18]. (d) High-resolution PSD of the diamond OMC acoustic "flapping" mode centered at $\omega_m/2\pi = 5.52$ GHz. The Lorentzian fit (solid red curve) estimates a mechanical Q-factor of ~4100. (e) PSDs of the acoustic flapping mode and optical transmission (white circles) plotted versus input laser wavelength, indicating significant optomechanical transduction occurs with the laser detuned approximately $\pm \sim 45$ pm from the optical cavity resonance. A clear optical bistability is present in the optical cavity transmission spectrum. The (f) optically amplified mechanical loss rate and (g) optical spring-shifted mechanical frequency (gray circles) measured as a function of laser detuning at a constant intercavity photon number of $n_c = 10,000$. The optical transmission spectrum (blue circles) is also plotted, with vertical gray dashed lines indicating $\Delta = \pm\omega_m$. Fits to (f) and (g) yield estimates of $\gamma_i/2\pi = 1.37$ MHz and $g_o/2\pi = 118$ kHz.

in Fig. 3(d)] of this feature reveals a Lorentzian mechanical resonance of the diamond OMC centered at $\omega_m/2\pi = 5.52$ GHz with a room temperature mechanical Q-factor of $Q_m \sim 4100$.

Given the measured optical cavity decay rate, our diamond OMC operates in the resolved sideband regime with $\omega_m/\kappa \sim 4.86$. In this regime, while the input laser is either red- or blue-detuned from the optical cavity by a mechanical frequency ($\Delta = (\omega_o - \omega_l) = \pm\omega_m$), the mechanical motion of the acoustic mode phase modulates the transmitted light, giving rise to a sideband of the input laser resonant with the optical cavity. The other first-order motional sideband, which is not resonant with the optical cavity, is suppressed in this scenario. As a result, the mechanical motion produces an intensity modulation in the RF power spectrum of the photoreceiver signal. To observe this effect directly, a weak input laser was tuned across the optical cavity at a constant power, while simultaneously monitoring the RF spectrum near the diamond OMC acoustic flapping mode. Figure 3(e) displays the collected spectra as a function of laser detuning, with the simultaneously collected optical transmission spectrum also plotted. A clear increase in optomechanical transduction is observed as the laser is tuned off-resonance from the optical cavity by $\pm \sim 45$ pm, corresponding to a detuning of approximately a mechanical frequency. Additionally, strong transduction occurs with the laser tuned within the cavity bandwidth, and a clear optical bistability is present in the optical cavity transmission spectrum. We attribute both observations to optical absorption (likely due to surface contamination), which causes a thermo-optic red shift in the optical resonance wavelength and an increase in the thermal Brownian motion of the mechanical cavity. To mitigate such thermal effects, a similar measurement was performed, but now with the input laser power continually adjusted via the VOA to maintain a constant intracavity photon number at each laser detuning [Figs. 3(f) and 3(g)]. From the measured optical cavity resonance frequency and linewidth, n_c is calculated by the relation

$$n_c = P_i \frac{\kappa_e/2}{\hbar\omega_l((\kappa/2)^2 + \Delta^2)}, \quad (1)$$

where P_i is the input laser power set by the VOA. In the resolved sideband limit [22], optomechanical backaction causes additional mechanical damping (γ_{OM}) and springing ($\delta\omega_m = |\omega_m - \omega_{m,o}|$) rates, respectively, of

$$\gamma_{\mathrm{OM}} = 2n_c|g_o|^2\,\mathrm{Re}\left[\frac{1}{i(\Delta-\omega_m)+\kappa/2}-\frac{1}{-i(\Delta+\omega_m)+\kappa/2}\right], \tag{2}$$

and

$$\delta\omega_m = n_c|g_o|^2\,\mathrm{Im}\left[\frac{1}{i(\Delta-\omega_m)+\kappa/2}-\frac{1}{-i(\Delta+\omega_m)+\kappa/2}\right]. \tag{3}$$

Under optimal detuning, with $\Delta = \pm\omega_m$, a maximum optomechanically induced damping rate of $\gamma_{\mathrm{OM}} = \pm 4n_c g_o^2/\kappa$ is expected. Figures 3(f) and 3(g) display the experimentally derived damping and springing curves (gray circles) for the diamond OMC acoustic flapping mode, respectively. A weak intracavity power, corresponding to $n_c \sim 10,000$ photons, was used for this measurement to avoid any thermal drifts in the cavity resonance. Indeed, the optomechanically induced damping is maximized (minimized) when the laser is detuned a mechanical frequency red (blue) of the optical cavity. Fits to these data sets, following Eqs. (2) and (3) (solid red lines), gave an estimate for the intrinsic mechanical damping of $\gamma_i/2\pi \sim 1.37$ MHz and the single-photon optomechanical coupling rate of $g_o/2\pi \sim 118$ kHz. This estimate differs only slightly from our design, which we attribute to uncertainty in the photoelastic constants of diamonds at telecom frequencies, as well as fabrication imperfections.

Figure 4(a) plots the measured mechanical linewidth of the diamond OMC acoustic flapping mode, collected under optimal red- and blue-sideband laser detuning as a function of the input power, up to the maximum output of the laser (in this case, corresponding to $n_c \sim 63,000$ photons). The effects of backaction are clearly visible, with the red-detuned laser ($\Delta = +\omega_m; \gamma_{\mathrm{red}}$) resulting in damping and the blue-detuned laser ($\Delta = -\omega_m; \gamma_{\mathrm{blue}}$) giving rise to anti-damping of the motion. From the mean value extracted from the γ_{red} and γ_{blue} data points, the estimated intrinsic mechanical linewidth is $\gamma_i/2\pi = 1.41 \pm 0.06$ MHz. The inset of Fig. 4(a) displays the optomechanically induced damping ($\gamma_{\mathrm{OM}} = \gamma_{\mathrm{red}} - \gamma_i$, black squares) plotted versus n_c. A linear fit to the γ_{OM} data yields $g_o/2\pi \sim 123 \pm 6$ kHz, which agrees well with the simulations and is consistent with previous estimates from the data plotted in Figs. 3(f) and 3(g). With the laser blue-detuned by a mechanical frequency, the threshold where $\gamma_{\mathrm{blue}} \sim 0$ is reached is at approximately $n_{c,\mathrm{thr}} \sim 27,000$, exciting the diamond OMC mechanical cavity into large amplitude optomechanical self-oscillations, so-called "phonon lasing" [14]. Mechanical spectra of the diamond OMC taken below, at, and above this phonon-lasing threshold [shown in Fig. 4(b)] show an over 70 dB increase in the peak mechanical amplitude [Fig. 4(b) inset].

The optomechanical cooperativity ($C \equiv \gamma_{\mathrm{OM}}/\gamma_i$) is plotted versus n_c in Fig. 4(c). To drive γ_{OM} beyond the level reached with the tunable laser output alone (i.e. to enable larger n_c), an EDFA was inserted before the VOA to increase the maximum input laser power. With the laser red-detuned by a mechanical frequency, a maximum cooperativity of $C \sim 6.6$ was reached for the acoustic flapping mode, as represented by the open squares in Fig. 4(b).

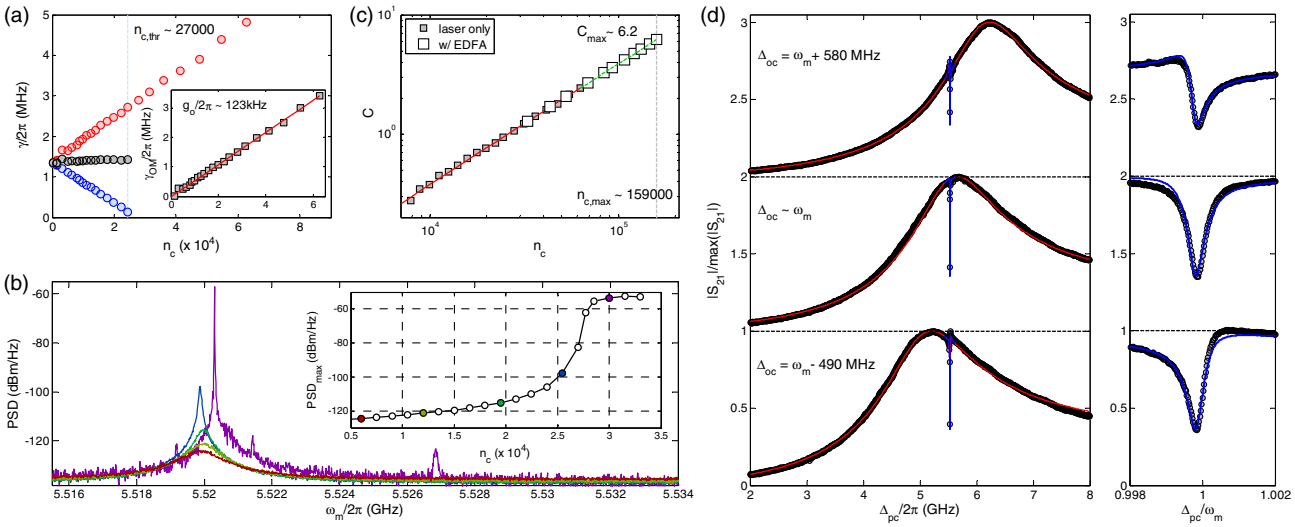

Fig. 4. Acoustic flapping mode "phonon lasing" and optomechanically induced transparency. (a) Measured mechanical linewidths (γ) collected at laser detuning of $\Delta = +\omega_m$ (γ_{red}, red circles) and $\Delta = -\omega_m$ (γ_{blue}, blue circles), up to the maximum laser power (corresponding to intracavity photon number of $n_c \sim 63,000$). Gray circles, which indicate the intrinsic mechanical linewidth values (γ_i) obtained by taking the average of the detuned data, yield an estimate of $\gamma_i/2\pi = 1.41 \pm 0.06$ MHz. The inset displays calculated optomechanically induced damping ($\gamma_{\mathrm{OM}} = \gamma_{\mathrm{red}} - \gamma_i$, gray squares), plotted versus n_c. A linear fit (red solid line) yields a coupling rate of $g_o/2\pi = 123 \pm 6$ kHz. Under blue laser detuning, a threshold input power of $n_{c,\mathrm{thr}} \sim 27,000$ (vertical blue dashed line) is required to observe phonon lasing of the mechanical cavity. (b) Normalized power spectral densities collected below, at, and above the phonon lasing threshold input power. The inset plots the peak PSD amplitude versus n_c, with a ~72 dB increase observed above threshold. (c) Cooperativity values ($C \equiv \gamma_{\mathrm{OM}}/\gamma_i$) collected under red laser detuning, plotted versus n_c. Solid gray squares and the linear fit (solid red line) are calculated from the γ_{OM} values shown in the panel (a) inset. Open gray squares correspond to mechanical spectra collected with the input laser amplified by an erbium doped fiber amplifier. The extrapolated linear fit (dashed green line) was used to infer the corresponding n_c values. (d) Normalized broadband OMIT spectra ($|S_{21}|/\max\{|S_{21}|\}$) collected with the control laser (ω_c) red detuned approximately $\Delta_{oc} \equiv (\omega_o - \omega_c) \sim [(\omega_m + 580\ \mathrm{MHz}), \omega_m, (\omega_m - 490\ \mathrm{MHz})]$, plotted versus probe laser (ω_p) detuning ($\Delta_{pc} \equiv (\omega_p - \omega_c)$). Right inset panels of (d) display zoomed-in OMIT spectra of the transparency window induced by coherent interaction of the mechanical and optical cavities. Fits to OMIT spectra [18] (solid red and blue lines) estimate a cooperativity of $C \sim 1.9$ for data collected with $\Delta_{oc} \sim \omega_m$.

Amplified spontaneous emission (ASE) optical noise output by the EDFA prevented a direct estimate of the intracavity photon number. However, from previous estimates of κ, γ_i, and g_o, a maximum intracavity photon number of $n_{c,\max} \sim 159,000$ was inferred (as indicated by the extrapolated dashed linear fit). Beyond this input power level, thermo-optic bistability shifts made it difficult to achieve precise laser detuning equal to a mechanical frequency. In relation to previously reported limits, diamond OMCs have an intracavity photon capacity nearly twice as large as OMC structures realized in silicon nitride [2,3].

With the demonstration of $C \gg 1$, optomechanical transduction in our diamond OMC acoustic flapping mode occurs at a substantially faster rate than energy loss of the system. This enables observations of the optomechanical analog to electromagnetically induced transparency, the so-called OMIT [9]. To observe OMIT in our diamond OMC structures, the input laser is red-detuned from the optical cavity and fixed as a strong driving control field (ω_c), while a weak probe field (ω_p, realized as sidebands created by an EOPM) is swept in frequency across the optical cavity resonance. Under optimal detuning conditions, whereby the control laser detuning equals a mechanical frequency ($\Delta_{oc} \equiv (\omega_o - \omega_c) = \omega_m$) and the probe-control detuning satisfies a two-photon resonance condition ($\Delta_{pc} \equiv (\omega_p - \omega_c) = \Delta_{oc}$), destructive interference of probe photons with control photons scattered by the mechanical resonator occurs. This yields a transparency window on the optical cavity transmission spectra, with its bandwidth set by the mechanical damping rate. A central requirement for this scattering phenomenon is that the probe and phonon-scattered photons are phase coherent, which demonstrates a coherent interaction of the mechanical resonator with the optical cavity. As previously mentioned, OMIT in our diamond OMC structures is observed via an $|S_{21}|$ measurement with a VNA [Fig. 3(a)], where port 1 of the VNA drives the EOPM input to create the weak probe field, which sweeps across the optical cavity, and port 2 collects the RF output of the high-speed photoreceiver. Figure 4(d) displays a representative series of normalized OMIT spectra ($|S_{21}|/\max\{|S_{21}|\}$) collected with the control laser detuned approximately $\Delta_{oc} \sim [(\omega_m - 490\ \text{MHz}), \omega_m, (\omega_m + 580\ \text{MHz})]$, and an intracavity photon number of $n_c \sim 59,000$. In these broadband OMIT spectra, we observe a clear dip representing the transparency window [right inset panels of Fig. 4(d) display zoomed-in spectra of this fine feature]. Fits to the normalized OMIT spectra [18], which followed the methodology reported previously [2,3], estimate a cooperativity of $C \sim 1.9$ for data collected with optimal $\Delta_{oc} \sim \omega_m$ detuning, in good agreement with the cooperativity value measured in Fig. 4(c) under a similar input laser power.

In addition to the resonance feature at ~5.5 GHz, two sharp features are also observed in the diamond OMC broadband thermal Brownian motion RF spectrum [Fig. 3(c)] near ~9.5 GHz. Figure 5(a) displays a zoomed-in RF spectrum around these features, collected with a weak laser signal slightly detuned from the optical cavity resonance. Four clear resonances are present in this span, with the central feature at ~9.5 GHz most strongly transduced by the optical cavity field. A high-resolution RF spectrum [shown in Fig. 5(b)] of this feature reveals a Lorentzian mechanical resonance of the diamond OMC centered at $\omega_m/2\pi = 9.45$ GHz with a mechanical Q-factor of $Q_m \sim 7700$. This corresponds to an $f \cdot Q$ product of $\sim 7.3 \times 10^{13}$ Hz, which is among the highest demonstrated for either bulk or small-scale single-crystal diamond mechanical oscillators at room temperature [23,24].

As before, we extract the optomechanical coupling rate for this mode by tuning the laser across the optical cavity resonance while maintaining a constant intracavity photon number of $n_c \sim 6000$ and simultaneously monitoring the mechanical resonance at 9.45 GHz. Fitting Eqs. (2) and (3) to the collected mechanical linewidth and frequency data [displayed in Figs. 5(c) and 5(d), respectively] yields an estimate for the intrinsic mechanical damping of $\gamma_i/2\pi \sim 1.18$ MHz and the single-photon optomechanical coupling rate of $g_o/2\pi \sim 239$ kHz. This value, as well as that of the mechanical resonance frequency, is in good agreement with

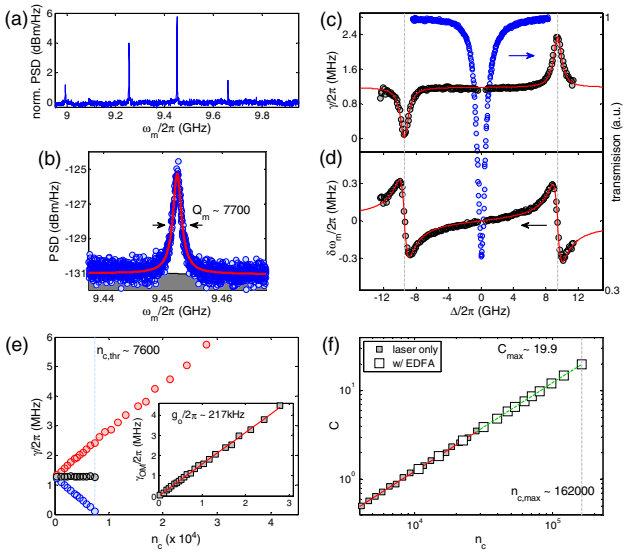

Fig. 5. Acoustic swelling mode mechanical spectroscopy. (a) Normalized power spectral density revealing a zoomed-in radio frequency spectrum of optically transduced diamond OMC thermal Brownian motion near ~9.5 GHz. (b) High-resolution PSD of the diamond OMC acoustic "swelling" mode centered at $\omega_m/2\pi = 9.454$ GHz. The Lorentzian fit (solid red curve) estimates a $Q_m \sim 7700$, corresponding to an $f \cdot Q$ product of $\sim 7.3 \times 10^{13}$ Hz. The (c) optically amplified mechanical loss rate and (d) optical spring-shifted mechanical frequency measured as a function of the laser detuning frequency at a constant intercavity photon number of $n_c = 6000$. The optical transmission spectrum (blue circles) is also plotted, with vertical gray dashed lines indicating $\Delta = \pm\omega_m$. Fits to (c) and (d) (red solid lines) yield estimates of $\gamma_i/2\pi = 1.18$ MHz and $g_o/2\pi = 239$ kHz. (e) Measured mechanical linewidths (γ) collected at laser detuning of $\Delta = +\omega_m$ (red circles) and $\Delta = -\omega_m$ (blue circles). Gray circles, which indicate the intrinsic mechanical linewidth values (γ_i) obtained by taking the average of the detuned data, yield an estimate of $\gamma_i/2\pi = 1.27 \pm 0.02$ MHz. The inset displays calculated optomechanically induced damping ($\gamma_{\text{OM}} = \gamma_{\text{red}} - \gamma_i$, black squares), plotted versus intracavity photon number (n_c). A linear fit (red solid line) yields $g_o/2\pi = 217 \pm 12$ kHz. Under blue laser detuning, an threshold input power of $n_{c,\text{thr}} \sim 7,600$ (vertical blue dashed line) is required to observe phonon lasing of the mechanical cavity. (f) Cooperativity values ($C \equiv \gamma_{\text{OM}}/\gamma_i$) collected under red laser detuning, plotted versus n_c. Solid gray squares and the linear fit (solid red line) are calculated from the γ_{OM} values shown the panel (e) inset. Open gray squares correspond to mechanical spectra collected with the input laser amplified by an erbium doped fiber amplifier. The extrapolated linear fit (dashed green line) was used to infer the corresponding n_c values. A maximum cooperativity value of $C \sim 19.9$ was measured at an estimated $n_c \sim 162,000$ (vertical dashed gray line).

the simulation results obtained for the diamond OMC acoustic swelling mode shown in Fig. 1(e). Repeating similar measurements on the other ∼9.5 GHz resonances observed in Fig. 5(a) confirmed the mechanical mode at $\omega_m/2\pi = 9.45$ GHz couples most strongly to the optical cavity. We believe that these additional resonances are likely of similar modal character, but hybridized with guided body modes of the diamond OMC, given the lack of isolation in an acoustic quasi-bandgap [25].

Figure 5(e) plots the measured mechanical linewidth of the diamond OMC acoustic swelling mode, collected under optimal red- and blue-sideband laser detuning ($\Delta = \pm\omega_m$) as a function of the input power, up to the maximum output of the laser, as well as with the amplified laser pump. In this instance, with the increased sideband resolution of $\omega_m/\kappa \sim 8.5$, the maximum laser power output corresponds to only $n_c \sim 29,000$ photons. The mean value extracted from the γ_{red} and γ_{blue} data points yields an estimated intrinsic mechanical linewidth of $\gamma_i/2\pi = 1.27 \pm 0.02$ MHz. A plot of the optomechanical cooperativity versus n_c, shown in Fig. 5(b), yields a second estimate for the optomechanical coupling rate of $g_o/2\pi \sim 217 \pm 12$ kHz, which is consistent with previous estimates for the diamond OMC acoustic swelling mode. From Fig. 5(f), the threshold power for the observation of optomechanical self-oscillations [18] under optimal blue-detuning was only $n_{c,\mathrm{thr}} \sim 7600$. Under optimal red-detuned laser conditions, the increased laser power afforded by the input EDFA enabled us to reach a room temperature mechanical linewidth $\gamma_{\mathrm{red}}/2\pi \sim 26.7$ MHz, which corresponds to a maximum observed cooperativity of $C \sim 19.9$ [Fig. 5(f)]. With previous estimates of κ, γ_i, and g_o for this acoustic swelling mode, an intracavity photon number of $n_c \sim 162,000$ was inferred at this cooperativity level. Thus, the much larger maximum cooperativity value measured for this acoustic swelling mode relative to the flapping mode is primarily the result of the increased optomechanical coupling rate. As before, higher cooperativities were not observed due to instabilities in the measurement under the high optical input power. OMIT was also observed for this acoustic swelling mode [18].

4. CONCLUSIONS

In summary, we have demonstrated resolved sideband cavity-optomechanics in a single-crystal diamond operating in the few to ∼10 GHz range, where optomechanical coupling via radiation pressure was sufficient to reach a room temperature cooperativity of nearly ∼20 for an intracavity photon population on the order of 10^5. Present devices also offer a promising platform for reaching much larger cooperativities when, for instance, operated at cryogenic temperatures, where mechanical Q-factors of diamond resonators have been shown to improve significantly [13]. Moreover, incorporating diamond color centers with monolithic OMCs is an interesting route to applications in quantum-nonlinear optomechanics. Diamonds are rich in optically active defects (color centers), such as the nitrogen-vacancy (NV) and silicon-vacancy (SiV) center, which behave as atom-like systems in the solid state [26,27]. Recent experiments [23,28–34] exploring coherent coupling of the NV electronic spin to phonons in mechanical resonators via lattice strain have demonstrated manipulation of the NV spin state at large driven mechanical amplitudes but remain far below the strong spin-phonon coupling regime. One way to boost this interaction would be to engineer truly nanoscale resonators, with feature sizes of a few hundred nanometers, and with frequencies in the hundreds of MHz to few GHz range. Such mechanical modes would provide a large change in the local strain per phonon [31]. The localized phononic modes of OMCs not only satisfy these requirements [35], with critical dimensions (i.e., the width of dielectric bridges between subsequent air holes) already in the order of ∼200 nm, but also are conveniently actuated and transduced with optical fields in the well-established telecom wavelength range. Diamond OMCs with coupled color centers may ultimately be used to map nonclassical spin qubit states as well as quantum states of light onto phonons and vice versa [36], and they will enable fundamentally new ways to prepare, control, and read out the quantum states of diamond spin qubits. Lastly, individual diamond OMCs integrated into larger arrays coupled through phononic waveguides [25] could enable long-range spin–spin interactions mediated by phonons [37].

We note that, parallel to this work, Mitchell *et al.* have demonstrated cavity optomechanics in single-crystal diamond microdisks [38].

Funding. Office of Naval Research (ONR) (N00014-15-1-2761); Air Force Office of Scientific Research (AFOSR) (FA9550-12-1-0025); Defense Advanced Research Projects Agency (DARPA) (PHY-0969816); National Science Foundation (NSF) (PHY-1125846, ECS-0335765, DMR-1231319); Institute for Quantum Information and Matter; Gordon and Betty Moore Foundation; Kavli Nanoscience Institute at Caltech; Harvard Quantum Optics Center (HQOC); Agency for Science, Technology and Research (A*STAR); Fondation Zdenek et Michaela Bakala.

Acknowledgment. The Institute for Quantum Information and Matter is an NSF Physics Frontiers Center with support from the Gordon and Betty Moore Foundation. M. J. Burek and H. A. Atikian were supported in part by the Harvard Quantum Optics Center (HQOC). C. Chia was supported in part by Singapore's Agency for Science, Technology and Research (A*STAR). T. Ruelle was supported in part by the Fondation Zdenek et Michaela Bakala. This work was performed in part at the Center for Nanoscale Systems (CNS), a member of the National Nanotechnology Infrastructure Network (NNIN), which is supported by the National Science Foundation award ECS-0335765. CNS is part of Harvard University. The authors would like to thank Y.-I. Sohn and V. Venkataraman for the useful discussions.

See Supplement 1 for supporting content.

REFERENCES AND NOTES

1. M. Eichenfield, J. Chan, R. M. Camacho, K. J. Vahala, and O. Painter, "Optomechanical crystals," Nature **462**, 78–82 (2009).
2. M. Davanço, S. Ates, Y. Liu, and K. Srinivasan, "Si_3N_4 optomechanical crystals in the resolved-sideband regime," Appl. Phys. Lett. **104**, 041101 (2014).
3. K. E. Grutter, M. Davanco, and K. Srinivasan, "Si3N4 nanobeam optomechanical crystals," IEEE J. Sel. Top. Quantum Electron. **21**, 61–71 (2015).
4. L. Fan, X. Sun, C. Xiong, C. Schuck, and H. X. Tang, "Aluminum nitride piezo-acousto-photonic crystal nanocavity with high quality factors," Appl. Phys. Lett. **102**, 153507 (2013).
5. A. Vainsencher, K. J. Satzinger, G. A. Peairs, and A. N. Cleland, "Bi-directional conversion between microwave and optical frequencies in

a piezoelectric optomechanical device," Appl. Phys. Lett. **109**, 033107 (2016).
6. K. C. Balram, M. Davanço, J. Y. Lim, J. D. Song, and K. Srinivasan, "Moving boundary and photoelastic coupling in GaAs optomechanical resonators," Optica **1**, 414–420 (2014).
7. K. C. Balram, M. I. Davanço, J. D. Song, and K. Srinivasan, "Coherent coupling between radiofrequency, optical and acoustic waves in piezo-optomechanical circuits," Nat. Photonics **10**, 346–352 (2016).
8. J. Chan, T. P. M. Alegre, A. H. Safavi-Naeini, J. T. Hill, A. Krause, S. Groblacher, M. Aspelmeyer, and O. Painter, "Laser cooling of a nanomechanical oscillator into its quantum ground state," Nature **478**, 89–92 (2011).
9. A. H. Safavi-Naeini, T. P. M. Alegre, J. Chan, M. Eichenfield, M. Winger, Q. Lin, J. T. Hill, D. E. Chang, and O. Painter, "Electromagnetically induced transparency and slow light with optomechanics," Nature **472**, 69–73 (2011).
10. A. H. Safavi-Naeini, S. Groblacher, J. T. Hill, J. Chan, M. Aspelmeyer, and O. Painter, "Squeezed light from a silicon micromechanical resonator," Nature **500**, 185–189 (2013).
11. J. T. Hill, A. H. Safavi-Naeini, J. Chan, and O. Painter, "Coherent optical wavelength conversion via cavity optomechanics," Nat. Commun. **3**, 1196 (2012).
12. S. E. Coe and R. S. Sussmann, "Optical, thermal and mechanical properties of CVD diamond," Diamond Relat. Mater. **9**, 1726–1729 (2000).
13. Y. Tao, J. M. Boss, B. A. Moores, and C. L. Degen, "Single-crystal diamond nanomechanical resonators with quality factors exceeding one million," Nat. Commun. **5**, 3638 (2014).
14. I. S. Grudinin, H. Lee, O. Painter, and K. J. Vahala, "Phonon laser action in a tunable two-level system," Phys. Rev. Lett. **104**, 083901 (2010).
15. M. J. Burek, Y. Chu, M. S. Z. Liddy, P. Patel, J. Rochman, S. Meesala, W. Hong, Q. Quan, M. D. Lukin, and M. Lončar, "High quality-factor optical nanocavities in bulk single-crystal diamond," Nat. Commun. **5**, 5718 (2014).
16. M. J. Burek, N. P. de Leon, B. J. Shields, B. J. M. Hausmann, Y. Chu, Q. Quan, A. S. Zibrov, H. Park, M. D. Lukin, and M. Lončar, "Free-standing mechanical and photonic nanostructures in single-crystal diamond," Nano Lett. **12**, 6084–6089 (2012).
17. P. Latawiec, M. J. Burek, Y.-I. Sohn, and M. Lončar, "Faraday cage angled-etching of nanostructures in bulk dielectrics," J. Vac. Sci. Technol. B **34**, 041801 (2016).
18. See Supplement 1 for details on simulations, fabrication, experimental setups, and data analysis.
19. J. Chan, A. H. Safavi-Naeini, J. T. Hill, S. Meenehan, and O. Painter, "Optimized optomechanical crystal cavity with acoustic radiation shield," Appl. Phys. Lett. **101**, 081115 (2012).
20. M. Eichenfield, J. Chan, A. H. Safavi-Naeini, K. J. Vahala, and O. Painter, "Modeling dispersive coupling and losses of localized optical and mechanical modes in optomechanical crystals," Opt. Express **17**, 20078–20098 (2009).
21. A. R. Lang, "The strain-optical constants of diamond: a brief history of measurements," Diamond Relat. Mater. **18**, 1–5 (2009).
22. A. H. Safavi-Naeini, J. Chan, J. T. Hill, S. Gröblacher, H. Miao, Y. Chen, M. Aspelmeyer, and O. Painter, "Laser noise in cavity-optomechanical cooling and thermometry," New J. Phys. **15**, 035007 (2013).
23. E. R. MacQuarrie, T. A. Gosavi, N. R. Jungwirth, S. A. Bhave, and G. D. Fuchs, "Mechanical spin control of nitrogen-vacancy centers in diamond," Phys. Rev. Lett. **111**, 227602 (2013).
24. P. Rath, S. Ummethala, C. Nebel, and W. H. P. Pernice, "Diamond as a material for monolithically integrated optical and optomechanical devices," Phys. Status Solidi A **212**, 2385–2399 (2015).
25. K. Fang, M. H. Matheny, X. Luan, and O. Painter, "Optical transduction and routing of microwave phonons in cavity-optomechanical circuits," Nat. Photonics **10**, 489–496 (2016).
26. I. Aharonovich, S. Castelletto, D. A. Simpson, C. H. Su, A. D. Greentree, and S. Prawer, "Diamond-based single-photon emitters," Rep. Prog. Phys. **74**, 076501 (2011).
27. A. Sipahigil, R. E. Evans, D. D. Sukachev, M. J. Burek, J. Borregaard, M. K. Bhaskar, C. T. Nguyen, J. L. Pacheco, H. A. Atikian, C. Meuwly, R. M. Camacho, F. Jelezko, E. Bielejec, H. Park, M. Lončar, and M. D. Lukin, "An integrated diamond nanophotonics platform for quantum optical networks," Science (to be published).
28. P. Ovartchaiyapong, K. W. Lee, B. A. Myers, and A. C. B. Jayich, "Dynamic strain-mediated coupling of a single diamond spin to a mechanical resonator," Nat. Commun. **5**, 4429 (2014).
29. E. R. MacQuarrie, T. A. Gosavi, A. M. Moehle, N. R. Jungwirth, S. A. Bhave, and G. D. Fuchs, "Coherent control of a nitrogen-vacancy center spin ensemble with a diamond mechanical resonator," Optica **2**, 233–238 (2015).
30. J. Teissier, A. Barfuss, P. Appel, E. Neu, and P. Maletinsky, "Strain coupling of a nitrogen-vacancy center spin to a diamond mechanical oscillator," Phys. Rev. Lett. **113**, 020503 (2014).
31. S. Meesala, Y.-I. Sohn, H. A. Atikian, S. Kim, M. J. Burek, J. T. Choy, and M. Lončar, "Enhanced strain coupling of nitrogen vacancy spins to nanoscale diamond cantilevers," Phys. Rev. Appl. **5**, 034010 (2015).
32. D. A. Golter, T. Oo, M. Amezcua, K. A. Stewart, and H. Wang, "Optomechanical quantum control of a nitrogen-vacancy center in diamond," Phys. Rev. Lett. **116**, 143602 (2016).
33. D. A. Golter, T. Oo, M. Amezcua, I. Lekavicius, K. A. Stewart, and H. Wang, "Coupling a surface acoustic wave to an electron spin in diamond via a dark state," arXiv:1608.01356 (2016).
34. E. R. MacQuarrie, M. Otten, S. K. Gray, and G. D. Fuchs, "Cooling a mechanical resonator with a nitrogen-vacancy center ensemble using a room temperature excited state spin-strain interaction," arXiv:1605.07131 (2016).
35. L. Kipfstuhl, F. Guldner, J. Riedrich-Möller, and C. Becher, "Modeling of optomechanical coupling in a phoxonic crystal cavity in diamond," Opt. Express **22**, 12410–12423 (2014).
36. S. D. Bennett, N. Y. Yao, J. Otterbach, P. Zoller, P. Rabl, and M. D. Lukin, "Phonon-induced spin-spin interactions in diamond nanostructures: application to spin squeezing," Phys. Rev. Lett. **110**, 156402 (2013).
37. K. Stannigel, P. Rabl, A. S. Sørensen, P. Zoller, and M. D. Lukin, "Optomechanical transducers for long-distance quantum communication," Phys. Rev. Lett. **105**, 220501 (2010).
38. M. Mitchell, B. Khanaliloo, D. P. Lake, T. Masuda, J. P. Hadden, and P. E. Barclay, "Single-crystal diamond low-dissipation cavity optomechanics," Optica **3**, 963–970 (2016).